ADVANCED MATERIALS
www.advmat.de

A CO_2-Tolerant Perovskite Oxide with High Oxide Ion and Electronic Conductivity

*Ming Li, Hongjun Niu, John Druce, Helena Téllez, Tatsumi Ishihara, John A. Kilner, Hripsime Gasparyan, Michael J. Pitcher, Wen Xu, J. Felix Shin, Luke M. Daniels, Leanne A. H. Jones, Vin R. Dhanak, Dingyue Hu, Marco Zanella, John B. Claridge, and Matthew J. Rosseinsky**

Mixed ionic–electronic conductors (MIECs) that display high oxide ion conductivity (σ_o) and electronic conductivity (σ_e) constitute an important family of electrocatalysts for a variety of applications including fuel cells and oxygen separation membranes. Often MIECs exhibit sufficient σ_e but inadequate σ_o. It has been a long-standing challenge to develop MIECs with both high σ_o and stability under device operation conditions. For example, the well-known perovskite oxide $Ba_{0.5}Sr_{0.5}Co_{0.8}Fe_{0.2}O_{3-\delta}$ (BSCF) exhibits exceptional σ_o and electrocatalytic activity. The reactivity of BSCF with CO_2, however, limits its use in practical applications. Here, the perovskite oxide $Bi_{0.15}Sr_{0.85}Co_{0.8}Fe_{0.2}O_{3-\delta}$ (BiSCF) is shown to exhibit not only exceptional bulk transport properties, with a σ_o among the highest for known MIECs, but also high CO_2 tolerance. When used as an oxygen separation membrane, BiSCF displays high oxygen permeability comparable to that of BSCF and much higher stability under CO_2. The combination of high oxide transport properties and CO_2 tolerance in a single-phase MIEC gives BiSCF a significant advantage over existing MIECs for practical applications.

Mixed ionic–electronic conductors (MIECs) that combine the required intrinsic transport properties of high oxide ion conductivity (σ_o) and electronic conductivity (σ_e) with high stability under device operation conditions are needed to accelerate the commercialization of a variety of electrochemical technologies. For example, oxy-fuel combustion coupled with MIEC oxygen separation membranes offers an economically viable solution for CO_2 capture and storage (CCS) for fossil-fuel fired power plants.[1,2] This technology involves combustion of fuels in pure oxygen, or in a mixture of oxygen balanced with recycled flue gas, producing a flue gas with a high concentration of CO_2 that allows easier sequestration without energy-intensive preprocessing. The MIEC membranes can provide pure oxygen with a reduced energy penalty and cost compared to conventional cryogenic air separation technology.[1] For this application, both high oxygen permeability and CO_2-tolerance of membranes are required to achieve the lowest energy penalties for CCS.[1]

To achieve high oxygen permeability, the MIECs should exhibit both high σ_o and σ_e to enhance bulk oxide mobility and oxygen surface exchange kinetics. However, in practice oxygen permeability is often limited by inadequate σ_o. Many important MIECs such as $La_{0.6}Sr_{0.4}Co_{0.2}Fe_{0.8}O_{3-\delta}$ (LSCF)[3–6] and $Ba_{0.5}Sr_{0.5}Co_{0.8}Fe_{0.2}O_{3-\delta}$ (BSCF)[7–10] are based on the ABO_3 perovskite oxide structure, in which oxygen ions migrate through the so-called saddle point defined between two A-site ions and a B-site ion.[11] Large A-site cations with high polarizability are helpful to achieve high σ_o by expanding the lattice to open the structural bottlenecks while screening variations in charge distribution produced by ionic motion that might otherwise self-trap the mobile species. $Ba_{0.5}Sr_{0.5}Co_{0.8}Fe_{0.2}O_{3-\delta}$ (BSCF), with a high concentration of the large and highly polarizable Ba^{2+} cation (Shannon dielectric polarizability 6.40 Å^3)[12] at the A-site, displays fast bulk oxide transport.

Dr. M. Li,[+] Dr. H. Niu, Dr. H. Gasparyan, Dr. M. J. Pitcher, W. Xu, Dr. J. F. Shin, Dr. L. M. Daniels, D. Hu, Dr. M. Zanella, Dr. J. B. Claridge, Prof. M. J. Rosseinsky
Department of Chemistry
University of Liverpool
Crown Street, Liverpool L69 7ZD, UK
E-mail: m.j.rosseinsky@liverpool.ac.uk

The ORCID identification number(s) for the author(s) of this article can be found under https://doi.org/10.1002/adma.201905200.

[+]Present address: Faculty of Engineering, University of Nottingham, University Park, Nottingham, NG7 2RD

Dr. J. Druce, Dr. H. Téllez, Prof. T. Ishihara, Prof. J. A. Kilner
International Institute for Carbon-Neutral Energy Research (wpi-I2CNER)
Kyushu University
744 Motooka, Nishi-ku, Fukuoka 819-0395, Japan

Prof. J. A. Kilner
Department of Materials
Imperial College London
London SW7 2AZ, UK

L. A. H. Jones, Prof. V. R. Dhanak
Department of Physics and Stephenson Institute for Renewable Energy
University of Liverpool
Liverpool L69 7ZF, UK

DOI: 10.1002/adma.201905200

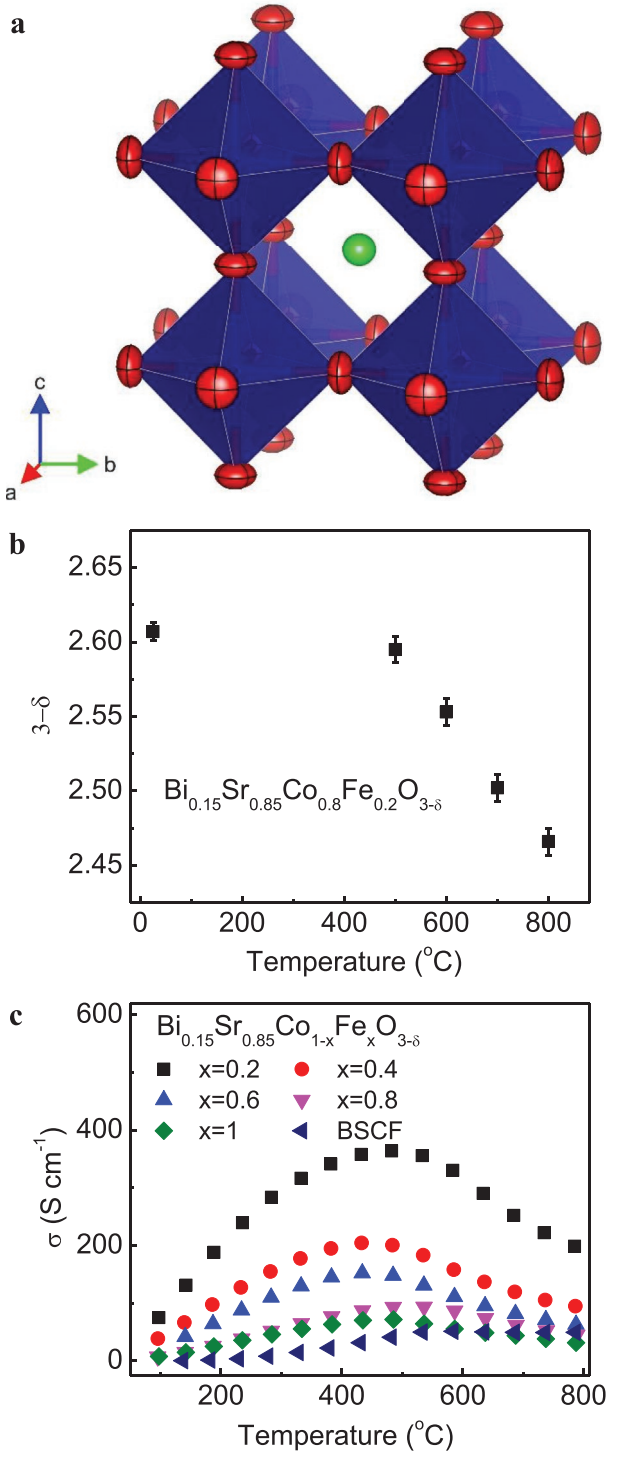

Figure 1. Structure, oxygen nonstoichiometry, and electrical conductivity. a) Crystal structure of $Bi_{0.15}Sr_{0.85}Co_{0.8}Fe_{0.2}O_{3-\delta}$ refined from neutron powder diffraction at 800 °C in air. All atoms are shown as 50% probability ellipsoids (green = Bi/Sr, blue = Co/Fe, and red = O), with the coordination environments of Co/Fe displayed as blue octahedra. b) Oxygen content of $Bi_{0.15}Sr_{0.85}Co_{0.8}Fe_{0.2}O_{3-\delta}$ as a function of temperature obtained by refinement against neutron powder diffraction data. c) Total electrical conductivity (σ) in air of $Bi_{0.15}Sr_{0.85}Co_{1-x}Fe_xO_{3-\delta}$ as a function of temperature. The electrical conductivity of $Ba_{0.5}Sr_{0.5}Co_{0.8}Fe_{0.2}O_{3-\delta}$ (BSCF) was also measured and is shown by the navy triangles for direct comparison.

The σ_o of BSCF calculated from the oxygen diffusion coefficient D^* is 0.07–0.17 S cm^{-1} at 600 °C[7–9] and 0.24 S cm^{-1} at 700 °C,[8] among the highest for known MIEC perovskite oxides,[7–9] giving rise to remarkably high oxygen permeability when used in oxygen separation membranes.[10] However, MIECs with solely large alkaline earth ions such as Ba and Sr on the A-site (e.g., BSCF) have high basicity and have a tendency to react with CO_2, leading to a degradation in permeation performance.[13,14] Despite the exceptional σ_o and electrocatalytic performance of BSCF, this instability toward CO_2 limits application in oxygen separation membranes, especially in environments where CO_2 is prevalent such as in oxy-fuel combustion. Various dopants have been employed to increase CO_2 tolerance of BSCF but typically at the cost of reduced oxygen permeability.[2]

Here, the single-phase perovskite oxide $Bi_{0.15}Sr_{0.85}Co_{0.8}Fe_{0.2}O_{3-\delta}$ (BiSCF) is shown to retain the exceptional oxide transport properties of BSCF and simultaneously exhibit a high CO_2 tolerance. The $Bi_{1-x}Sr_xCo_{1-y}Fe_yO_{3-\delta}$ phases were selected based on a number of hypotheses below. First, the $6s^2$ electronic configuration gives Bi^{3+} a large Shannon dielectric polarizability (6.12 Å^3)[12] and a flexible oxide coordination chemistry supporting many Bi—O geometries[15] with low Bi—O bond strengths,[16] which have been shown to enable high oxygen mobility in a number of perovskite oxides.[17–24] Second, Bi doping is expected to increase CO_2 tolerance due to reduced basicity of Bi^{3+} oxides when compared against BSCF. Thermogravimetric (TGA) measurements under a CO_2 atmosphere show that $BaCO_3$ decomposes at ≈1340–1360 °C[25] whereas the decomposition of $Bi_2O_2CO_3$ begins at ≈400–430 °C, reflecting the reduced thermal stability of Bi^{3+} versus alkaline earth carbonates.[26] Third, bismuth surface enrichment has been observed in some bismuth-containing oxides.[27–29] It is hypothesized that a surface enriched in the less basic Bi^{3+} will also reduce reactivity to CO_2. These potential advantages of high oxygen mobility and reduced basicity lead to the exploration of $Bi_{1-x}Sr_xCo_{1-y}Fe_yO_{3-\delta}$ phases with the aim of coupling high σ_o with high CO_2 tolerance in a perovskite MIEC.

There are to date only a few reports in the literature on the $Bi_{1-x}Sr_xCo_{1-y}Fe_yO_{3-\delta}$ family.[30–34] The series of $Bi_{0.15}Sr_{0.85}Co_{1-x}Fe_xO_{3-\delta}$ ($0 \le x \le 1.0$) perovskite oxides were previously synthesized by quenching in air, with measurement of structural and magnetic properties, but no transport properties were reported.[35,36] In contrast to the quenching method used in the previous report,[36] all $Bi_{0.15}Sr_{0.85}Co_{1-x}Fe_xO_{3-\delta}$ ($0.2 \le x \le 1.0$) samples in the present work were furnace-cooled in air with a cooling rate of 5 °C min^{-1}. The X-ray diffraction (XRD, Figure S3, Supporting Information) and neutron powder diffraction (NPD, Figures S4 and S6, Tables S2 and S3, Supporting Information) patterns collected at room temperature and high temperatures (500–800 °C) can be indexed and refined based on the cubic $Pm\bar{3}m$ space group showing that $Bi_{0.15}Sr_{0.85}Co_{1-x}Fe_xO_{3-\delta}$ ($0.2 \le x \le 1.0$) is stable over this temperature range. The refined structure of $Bi_{0.15}Sr_{0.85}Co_{0.8}Fe_{0.2}O_{3-\delta}$ at 800 °C is shown in **Figure 1**a. The lattice parameters (a) at room temperature lie in the range 3.8838–3.9013 Å (Figure S3b, Supporting Information), close to the values reported previously[36] and smaller than that of BSCF (3.9730 Å, PDF Card No. 00-055-0563). As such, the A—O distances are shorter in BiSCF (2.7231 Å) than in BSCF (2.8228 Å). This will stabilize the oxide over the carbonate, consistent with the observation that larger cations stabilize salts with larger anions (carbonate

in this case) on ionic model lattice enthalpy grounds.[37] The bond valence sum for Sr^{2+} in BiSCF is 2.282 and is 2.116 for Bi^{3+} which are not too dissimilar from the expected 2.15 valence for the A site. This is contrasted with a larger average A site bond valence sum of 2.315 in BSCF and significant disparity between Sr^{2+} (1.786) and Ba^{2+} (2.843). The incorporation of Bi^{3+} in BiSCF introduces covalent bonding between A-site cations and oxygen, which reduces the ionic character of the A—O bond when compared with BSCF.

BiSCF exhibits considerable oxygen nonstoichiometry, with $\delta = 0.39(1)$ at room temperature and ambient oxygen partial pressure, which is significantly larger than that in LSCF ($\delta < 0.05$)[3,4] and slightly lower than that of BSCF ($\delta \approx 0.45$)[38] measured under similar conditions. The oxygen content ($3-\delta$) of BiSCF at high temperatures was determined using neutron diffraction, cerimetric titration, and TGA which all give consistent data (Table S4, Supporting Information). Upon heating from 500 to 800 °C, BiSCF releases oxygen and the oxygen content decreases to 2.466(9) at 800 °C (Figure 1b and Table S4, Supporting Information). This is a result of the temperature- and oxygen partial pressure (pO_2)-dependent equilibrium of the oxygen sublattice with the gas phase, where higher temperature entropically favors dioxygen gas, and is a common characteristic of perovskite oxides containing transition metals with variable valences such as Fe and Co.[4,39]

The $Bi_{0.15}Sr_{0.85}Co_{1-x}Fe_xO_{3-\delta}$ materials exhibit high total electrical conductivity (σ), which varies with temperature and Co/Fe ratio (Figure 1c). The compositions with higher Co contents exhibit higher σ. In particular, the $Bi_{0.15}Sr_{0.85}Co_{0.8}Fe_{0.2}O_{3-\delta}$ (BiSCF) composition shows a maximum σ of ≈365 S cm^{-1} at ≈500 °C, and σ remains close to 200 S cm^{-1} up to 800 °C. The maximum σ of BiSCF is comparable to that of LSCF (≈350–400 S cm^{-1})[3,4] and significantly higher than that of BSCF (≈50 S cm^{-1}, Figure 1c).

BiSCF also exhibits exceptionally high oxygen diffusivity, as revealed by ^{18}O tracer measurements using ceramic samples and the secondary ion mass spectrometry (SIMS)-line scan technique (**Figure 2**). The oxygen tracer diffusion coefficient, D^*, provides a direct and quantitative description of the oxygen transport properties. The D^* values of BiSCF are ≈1.4×10^{-7} and 7.2×10^{-7} cm^2 s^{-1} at 600 and 700 °C, respectively (Figure 2a). These D^* values are among the highest for the known perovskite oxides and compare well with those of BSCF and other MIECs (Figures S10 and S11, Supporting Information). For example, the D^* of BiSCF is approximately three orders of magnitude higher than that of LSCF at 600 °C (D^* is ≈2.2×10^{-10} at 594 °C for LSCF).[40] For the data collected using the line scan technique, the D^* value of BiSCF is slightly lower than that of BSCF at temperatures ≤600 °C (D^* values of BSCF ceramic[7] and thin film[8] samples are 3.0×10^{-7} to 3.6×10^{-7} cm^2 s^{-1} at ≈600 °C), but increases more rapidly with temperature and becomes higher than that of BSCF above 700 °C. The activation energy, E_a, for tracer diffusion in BiSCF is 1.2 eV, which is higher than the 0.5–1.1 eV for BSCF,[7,8] but lower than the ≈1.9 eV of LSCF.[40]

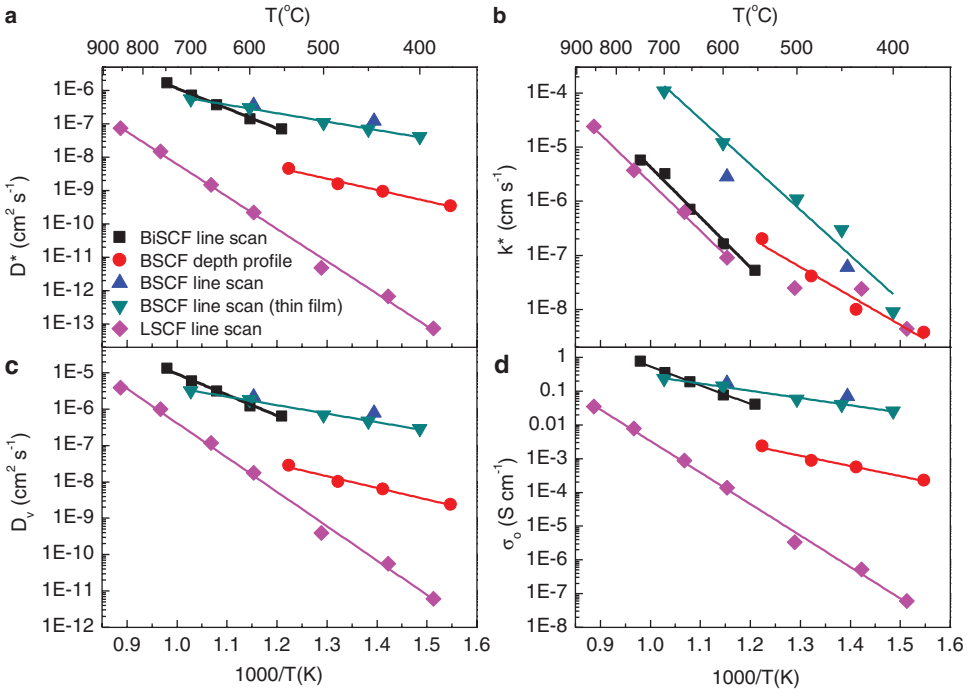

Figure 2. Bulk oxide transport properties and oxygen surface exchange kinetics. a) The oxygen tracer diffusion coefficient, D^*, b) the oxygen surface exchange coefficient, k^*, c) the oxygen vacancy diffusion coefficient, D_v, and d) the oxide ion conductivity (σ_o) of $Bi_{0.15}Sr_{0.85}Co_{0.8}Fe_{0.2}O_{3-\delta}$ (BiSCF) compared with $Ba_{0.5}Sr_{0.5}Co_{0.8}Fe_{0.2}O_{3-\delta}$ (BSCF)[7] and $La_{0.6}Sr_{0.4}Co_{0.2}Fe_{0.8}O_{3-\delta}$ (LSCF)[40] measured with ceramic samples using the SIMS-line scan technique. The exchange oxygen partial pressure (pO_2) is ≈0.21 bar for all ceramic samples including those from the literature. Data for BSCF ceramic samples measured using SIMS-depth profile within individual single grains[7] and BSCF thin film samples (exchange pO_2 is 0.5 bar) measured using SIMS-line scan[8] are also presented. Comparison with other known MIECs including $La_{0.3}Sr_{0.7}CoO_{3-\delta}$ (LSC), $GdBaCo_2O_{5+\delta}$ (GBCO) and $La_2NiO_{4+\delta}$ (LNO) is shown in Figures S10 and S11 (Supporting Information). Typical diffusion profiles and fits for isotope diffusion profiles at 600 and 650 °C are shown in Figure S12 (Supporting Information).

Since the oxide ion conduction is achieved via the migration of oxygen vacancies, the oxygen vacancy diffusion coefficient, D_v, is calculated from the measured D^* and oxygen content using Equations (S3) and (S4) (Supporting Information), and compared with other MIECs (Figure 2c and Figure S11a, Supporting Information). D_v of BiSCF is higher than that of LSCF (by 1–2 orders of magnitude at 550–750 °C) and compares favorably with that of BSCF above 600 °C (D_v at 700 °C = 5.9×10^{-6} cm^2 s^{-1} for BiSCF and 3.2×10^{-6} cm^2 s^{-1} for BSCF[8]).

The σ_o value, calculated via the Nernst–Einstein relationship (Equation (S5), Supporting Information) using the measured D^*, a correlation factor of 0.69 (for a cubic perovskite),[41] the oxygen content at the measurement temperature (Table S4, Supporting Information) and cell volume (Figure S3b, Supporting Information) reaches 0.077 S cm^{-1} at 600 °C and 0.35 S cm^{-1} at 700 °C (Figure 2d). In contrast, by using the reported D^* values,[40] and the oxygen content and cell volume,[3] the calculated σ_o of LSCF is $\approx 1.4 \times 10^{-4}$ S cm^{-1} at 594 °C, $\approx 8.7 \times 10^{-4}$ S cm^{-1} at 663 °C, and $\approx 7.9 \times 10^{-3}$ S cm^{-1} at 761 °C. Thus, σ_o of BiSCF is at least two orders of magnitude higher than that of LSCF at similar temperatures, and is comparable to that of BSCF below 700 °C; above this temperature it is even higher (Figure 2d and Figure S11b, Supporting Information).

BiSCF also exhibits rapid oxygen surface exchange kinetics (Figure 2b). At a pO_2 of 0.21 bar, the oxygen surface exchange coefficient (k^*) is $\approx 1.6 \times 10^{-7}$ and 3.2×10^{-6} cm s^{-1} at 600 and 700 °C, respectively. Reported k^* values strongly depend on measuring methods, sample form (thin film or ceramic), and exchange pO_2. There are often significant discrepancies in reported k^* values even for the same nominal composition, which can significantly depend upon the microstructure.[7,8] Nevertheless, overall, the k^* values measured for BiSCF are slightly higher than those found for LSCF ceramic samples[40] but about one order of magnitude lower than those for BSCF ceramic samples measured using the same technique with similar exchange pO_2. The E_a for k^* of BiSCF is 1.8 eV, which is close to that of LSCF (≈1.8 eV) measured above 600 °C.[40]

The chemical composition of the outer surface of the BiSCF ceramic strongly depends on the thermal history of the samples. Low-energy ion scattering (LEIS) is a highly surface-sensitive technique to determine the composition of the outermost atomic layer of a material and has been employed to study ceramic, thin film, or powder samples.[42–44] LEIS analysis of the BiSCF ceramic using 5 keV Ne^+ ions shows the presence of all the cations after polishing, as expected for the starting composition (**Figure 3**a). Thermal treatment leads to a significant segregation of both Sr and Bi cations (as shown by an increase of the peak areas at ≈2150 and 3526 eV, respectively), with a concomitant decrease of the B cations surface coverage (indicated by the disappearance of the (Fe + Co) peak at ≈1370 eV after annealing at 650 °C). These results are consistent with previous LEIS measurements on ceramic LSCF where the outermost atomic layer of LSCF consists of A-site cations rather than B-site cations.[42,45] However, the ratios of the A-site cations in the outermost atomic layer of BiSCF differ from those in LSCF.[42,45] In LSCF, the peak corresponding to lanthanum vanishes after annealing at high temperatures (>600 °C) and the outermost atomic layer is shown to contain only Sr.[42,45] In BiSCF, the outermost atomic layer still contains more Bi and less Sr than the bulk (Figure 3b), consistent with the Bi surface enrichment also observed with LEIS in Bi-based pyrochlores.[29]

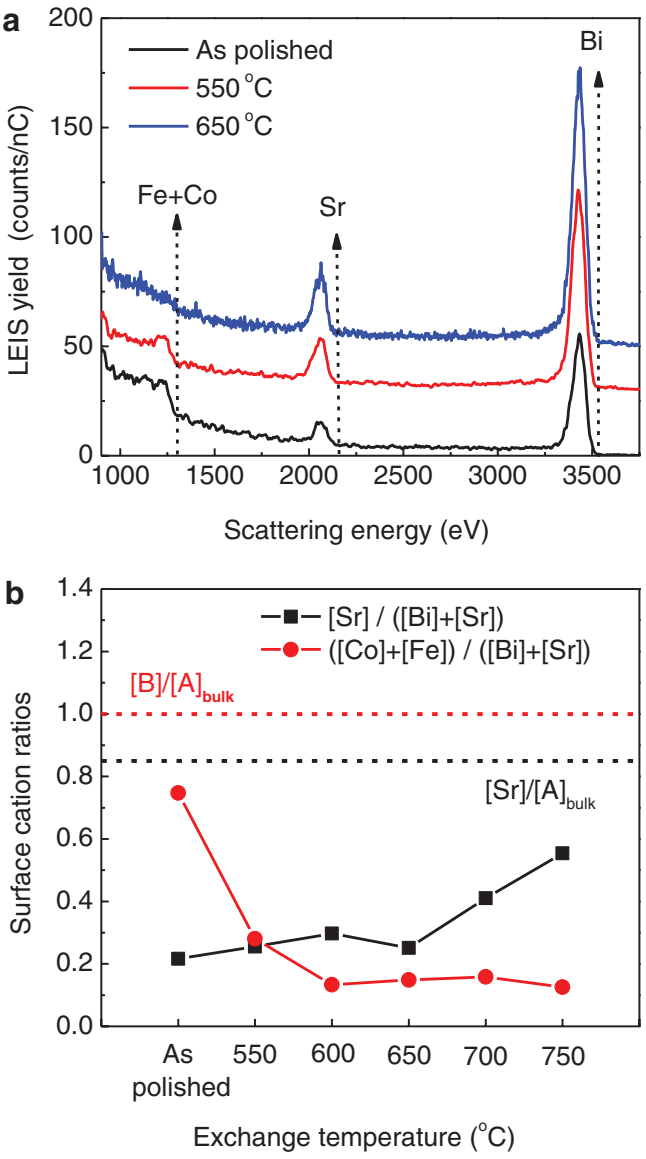

Figure 3. Surface composition. a) Low-energy ion scattering (LEIS) surface spectra obtained for 5 keV $^{20}Ne^+$ ions scattered by BiSCF samples as polished and after exchange at 550 and 650 °C. b) Surface cation ratios as a function of the exchange temperature as obtained from the 5 keV $^{20}Ne^+$ LEIS spectra.

The surface enrichment of Bi in BiSCF was also confirmed by X-ray photoelectron spectroscopy (XPS) data (Figure S13, Supporting Information). XPS has a typical sampling depth of 3–10 nm and is less surface sensitive than LEIS. The sampling depth could be reduced by lowering the emission angles at which the electrons are collected, which enables detection of compositions closer to the surface. The intensity of Bi 4f peaks increases with lowering emission angles from 90° to 70° and 60° (Figure S13, Supporting Information), implying higher Bi concentration closer to the surface. Although the XPS tests do not provide the accurate and quantitative composition analysis

for the outermost atomic layer of BiSCF, the XPS results qualitatively support the Bi surface enrichment as revealed by LEIS. As Bi^{3+} has a higher charge than Sr^{2+}, the Bi surface enrichment presumably decreases the surface oxygen vacancy concentration which may in turn explain why BiSCF, despite its high oxygen mobility, exhibits a lower k^* than BSCF at intermediate temperatures. Note that k^* depends on not only intrinsic material parameters such as oxygen mobility and oxygen vacancy concentration[46] but also surface microstructure.[47–49] The approach of surface microstructure engineering could be employed to further improve the k^* of BiSCF.

In addition to the exceptional bulk oxide transport properties, BiSCF also exhibits high CO_2 tolerance (**Figure 4**). Rapid weight gain was observed for BSCF (Figure 4a) due to reaction with CO_2 and formation of $(Ba,Sr)CO_3$ when heated in a CO_2-containing atmosphere ($70\%CO_2$–$20\%O_2$–$10\%Ar$) at 900 °C. The weight gain reached ≈10.0% after tests at 900 °C for 20 h. In sharp contrast, under the same test conditions the weight gain for BiSCF is only 0.35%. The XRD patterns (Figure 4b) reveal no observable $SrCO_3$ after test at 900 °C with 70% CO_2 for 20 h, whereas BSCF decomposed with significant formation of carbonates and CoO (Figure 4c).

The combination of high electrocatalytic performance and CO_2 tolerance of BiSCF was demonstrated through oxygen permeation measurements using 100% CO_2 sweep gas (Figure 4d). At high temperatures (950 °C) under He sweep gas, BiSCF exhibits a high oxygen permeation flux (JO_2) of 1.45 mL min^{-1} cm^{-2}, comparable to the 1.77 mL min^{-1} cm^{-2} obtained for BSCF. A sharp contrast between the CO_2 tolerance of BSCF and BiSCF was observed. Consistent with reports in the literature,[13,14] the JO_2 of BSCF at 875 °C dropped quickly to near-zero (<0.02 mL min^{-1} cm^{-2}) when pure CO_2 sweep gas was introduced. For BiSCF, the JO_2 at 950 °C dropped from 1.45 to 0.87 mL min^{-1} cm^{-2} after ≈100 h and then became stable. The JO_2 recovered quickly to 1.57 mL min^{-1} cm^{-2} after the sweep gas was switched back to pure helium. The decrease of JO_2 under CO_2 sweep gas and the recovery of JO_2 by switching the sweep gas from CO_2 to helium have been commonly observed in the literature for many MIEC membranes including BSCF and LSCF.[6,13,14] The decrease of JO_2 under CO_2 sweep gas is attributed to the formation of carbonate phases if there is severe reaction between CO_2 and MIEC material,[13,14] or to reduced oxygen vacancy concentration associated with CO_2 adsorption on the membrane surface where the chemical reaction between CO_2 and MIEC material is less severe (e.g., in the case of LSCF).[6] After switching the sweep gas from CO_2 back to helium, JO_2 recovers due to the decomposition of carbonate phases and/or desorption of CO_2 from the membrane surface.

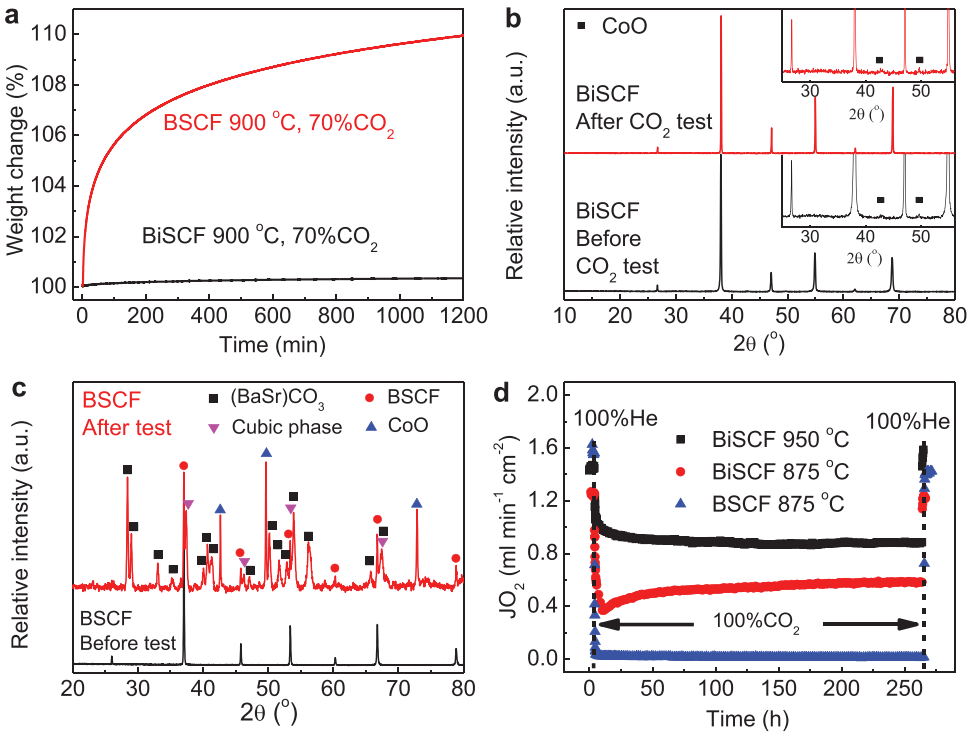

Figure 4. CO_2 tolerance and oxygen permeation. a) TGA data showing the weight gain due to reaction with CO_2 as a function of time for $Ba_{0.5}Sr_{0.5}Co_{0.8}Fe_{0.2}O_{3-\delta}$ (BSCF) and $Bi_{0.15}Sr_{0.85}Co_{0.8}Fe_{0.2}O_{3-\delta}$ (BiSCF) under $70\%CO_2$-$20\%O_2$-$10\%Ar$ at 900 °C. b) The XRD patterns of BiSCF after TGA tests in CO_2. The inset shows the expanded view of the CoO minority secondary phase, which is the same before and after the tests. c) The XRD patterns of BSCF after TGA tests in CO_2 showing significant decomposition of BSCF. The cubic phase (down-pointing triangle) has the BSCF-type structure but smaller lattice parameter. d) Oxygen permeation stability tests using 100% helium or CO_2 sweep gas for BiSCF and BSCF membranes. The membrane thickness is 1.0 mm. A BSCF membrane with the same thickness was also tested at 875 °C for direct comparison. At each temperature the JO_2 was initially tested in 100% helium. The sweep gas was then switched to 100% CO_2 for ≈260 h, before being finally changed back to 100% helium. The flow rate for the feed gas (21% O_2, 79% N_2) and sweep gas is 100 mL min^{-1}.

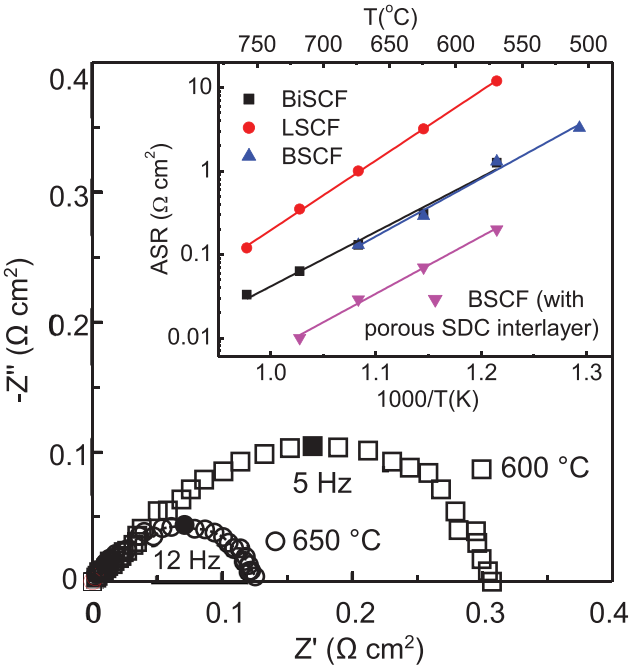

Figure 5. Electrocatalytic performance of BiSCF as a solid oxide fuel cell (SOFC) cathode. Typical impedance complex plane plots showing the area specific resistance (ASR) of BiSCF cathode at 600 and 650 °C. Filled symbols indicate selected frequencies. Note that the ohmic impedance associated with the LSGM electrolyte has been subtracted from the spectra (an original impedance complex plane plot is shown in Figure S16, Supporting Information). The ASR values shown in the inset were normalized for the electrode area and divided by 2 to account for the symmetry of the cell. Comparison with typical ASR values of BSCF[49] and LSCF[51] is shown in the inset.

During these processes the roughness of the membrane surface can increase, which increases the surface exchange kinetics, and therefore JO_2 returns to be above the initial value.[50]

After the tests at 950 °C, the temperature was decreased to 875 °C. The JO_2 at 875 °C with helium sweep gas was 1.25 mL min^{-1} cm^{-2}, which decreased to 0.37 mL min^{-1} cm^{-2} under CO_2 sweep gas, then recovered slowly to 0.58 mL min^{-1} cm^{-2} and became stable at this value during the 260 h test. The stable JO_2 values of BiSCF with pure CO_2 sweep gas at both 950 and 875 °C are higher than those of many other MIECs under similar test conditions.[2,14] After the tests at 875 °C, the temperature was increased to 950 °C. A 130 h test stability test in helium was performed. A stable JO_2 of 1.59 mL min^{-1} cm^{-2} was observed (Figure S14, Supporting Information).

The high electrocatalytic performance of BiSCF was also apparent in its performance as a solid oxide fuel cell (SOFC) cathode. Symmetrical cathode/electrolyte/cathode cells were fabricated using BiSCF as cathode and LSGM ($La_{0.80}Sr_{0.20}Ga_{0.80}Mg_{0.20}O_{2.8}$) as electrolyte. The area specific resistance (ASR) of the BiSCF cathode is as low as 0.31 and 0.13 Ω cm^2 at 600 and 650 °C, respectively (**Figure 5**, Figure S16 and Table S6, Supporting Information). The ASR values of BiSCF cathodes are about one order of magnitude lower than the typical values of LSCF[51–53] and are comparable to those of BSCF without interfacial/microstructural optimization,[49] demonstrating the high electrocatalytic performance exhibited by BiSCF. There is scope for further improvement to the ASR of BiSCF through optimization of the microstructure. For example, the ASR of BSCF cathode is decreased when a porous samarium-doped ceria (SDC) interlayer is deposited between the BSCF cathode and the SDC electrolyte.[49] The E_a of 1.3 eV is similar to that of BSCF and smaller than ≈1.7 eV of LSCF.

In summary, the substitution of the post-transition metal Bi^{3+} cation onto the A-site of the perovskite structure in BSCF retains similar oxygen vacancy content and bulk oxide ion conductivity, while also significantly increasing the stability to CO_2. As a result, BiSCF displays comparable electrocatalytic performance to BSCF in oxygen permeation membranes and SOFC cathodes, and, unlike BSCF, retains this performance in the presence of CO_2. The high polarizability and diverse oxide coordination chemistry characteristic of the Bi^{3+} "inert lone pair" outer shell electronic configuration confers comparable anion mobility while enhancing transition metal-oxide orbital overlap and electronic conductivity from the shorter B—O bonding. Furthermore, the more electropositive character of Bi^{3+} versus Ba^{2+} and Sr^{2+} decreases the basicity of the oxide anions in BiSCF below that in the alkaline-only A site BSCF where the ionic character of the A—O bond is higher, and thus reduces reactivity with Lewis acidic CO_2. This effect is amplified at the surface due to the locally increased Bi content. Together, these bulk and surface chemical effects allow BiSCF to largely retain its oxygen permeation performance in a pure CO_2 atmosphere, in stark contrast to BSCF. The work demonstrates an approach to achieve synergic tuning of the bulk and surface properties of a complex perovskite oxide mixed ionic–electronic conductor to couple high anion mobility with enhanced chemical stability.

Experimental Section

$Bi_{0.15}Sr_{0.85}Co_{1-x}Fe_xO_{3-\delta}$ (x = 0.2, 0.4, 0.6, 0.8, and 1.0) powders were prepared using a solid-state reaction route. Raw materials Bi_2O_3 (99.9%), $SrCO_3$ (99.994%), Co_3O_4 (99.7%), and Fe_2O_3 (99.998%) were dried, weighed, and mixed by ball milling. The raw material mixtures were calcined three times at 800, 950, and 1000 °C for 6 h each with heating and cooling rates of 1 and 5 °C min^{-1}, respectively. A further calcination at 1050 °C for 6 h for x = 0.8 and another calcination at 1100 °C for 6 h for x = 1 were carried out. Dense pellets were obtained by sintering at 1050–1150 °C (depending on composition) for 6 h with heating and cooling rates of 5 and 2 °C min^{-1}, respectively. All as-prepared pellets have high relative density (>95%).

The phase purity was examined using a Panalytical X'Pert Pro diffractometer with Co Kα_1 radiation. High-resolution time-of-flight (ToF) neutron powder diffraction patterns were collected from a powder sample contained in a thin-walled vanadium can at ambient temperature using the HRPD instrument at ISIS, UK. High-temperature ToF-NPD patterns were obtained from sintered pellets contained in a single-walled quartz gas-flow cell under flowing air, with data collected on warming in the range 500–800 °C using the Polaris instrument at ISIS, UK.

Ceramic microstructure and compositional analysis were performed using a Hitachi S-4800 field-emission scanning electron microscope (SEM) equipped with an Oxford INCA energy-dispersive X-ray spectroscopy (EDS) detector.

Cerimetric titration was used to determine the oxygen content in the as-prepared powder samples. The oxygen content at high temperatures

and in air were determined using three methods. The first approach was to refine the high-temperature in situ NPD data. For the second approach, the samples were quenched from the desired temperature into liquid nitrogen in less than 0.5 s using a home-made rig (Figure S1, Supporting Information). The oxygen content was then analyzed using the cerimetric titration method. The third approach was to first determine the oxygen content at 950 °C using the above quenching procedures. The oxygen contents at other desired temperatures were then obtained by measuring the weight difference between the desired temperature and 950 °C using TGA (TA Instruments SDT-Q600 TGA).

The CO_2-tolerance of BiSCF and BSCF was evaluated by measuring the weight gain as a function of time using TGA under 70%CO_2-20%O_2-10%Ar at 900 °C.

The compatibility with common electrolyte materials (SDC, $Sm_{0.2}Ce_{0.8}O_{1.9}$; LSGM, $La_{0.80}Sr_{0.20}Ga_{0.80}Mg_{0.20}O_{2.8}$; and YSZ, 8 mol% yttria stabilized zirconia) was evaluated by annealing the mixtures of BiSCF and electrolyte materials at 850 and 950 °C for 3 h. The phase purity after annealing was examined using XRD.

A Linseis LSR -3 Linseis Seebeck Coefficient & Electric Resistivity Unit was used to measure dc conductivity and Seebeck coefficient in air from 100 to 800 °C using bar-shaped samples.

Oxygen isotope exchanges were conducted according to standard isotope exchange protocols in a custom-built exchange setup. The preannealing step in normal oxygen was approximately ten times as long as the subsequent ^{18}O exchange anneal (Table S1, Supporting Information). The oxygen pressure for both normal O_2 anneal and isotopically enriched O_2 anneals was 200 mbar. After the isotope exchange, the oxygen isotope distribution was determined by ToF-SIMS (ToF-SIMS V, Ion-ToF GmbH., Germany) analysis of polished cross sections of each sample. Typical diffusion profiles and fits for isotope diffusion profiles at 600 and 650 °C are shown in Figure S12 (Supporting Information). The chemical composition of the outermost atomic layer of the BiSCF ceramic was analyzed by LEIS (Qtac^{100} Spectrometer, Ion-ToF GmbH, Germany).

Oxygen permeation measurements under an oxygen partial pressure gradient were performed in a Probostat (NorECs, Norway) measurement cell (Figure S2, Supporting Information). Oxygen permeation fluxes were measured using a PerkinElmer Clarus 580 gas chromatograph (GC) equipped with a thermal conductivity detector.

Symmetrical BiSCF/LSGM/BiSCF cells were fabricated by screen-printing BiSCF ink on LSGM. Gold wire and gauze were attached to both sides of the symmetrical cell using gold paste. ASR measurements were performed at 550–750 °C.

Full experimental section and any associated references are available in the Supporting Information.

Supporting Information

Supporting Information is available from the Wiley Online Library or from the author.

Acknowledgements

The authors thank the European Research Council (ERC) for support under RLUCIM (Grant Agreement No. 227987) and EPSRC for funding (EP/N004884/1). W.X. was supported by an EPSRC studentship. J.D., H.T., J.K., and T.I. acknowledge support from wpi-I2CNER, part of the MEXT "WPI" programme. Additionally, H.T. was supported by a JSPS Postdoctoral Fellowship from the Japan Society for the Promotion of Science (P13770). The authors thank Dr. Kevin Knight for assistance on HRPD and Dr. Ron Smith for assistance on Polaris.

Conflict of Interest

The authors declare no conflict of interest.

Keywords

mixed ionic–electronic conductors, oxygen separation membranes, perovskites, solid oxide fuel cells, surface segregation

Received: August 12, 2019
Revised: October 14, 2019
Published online:

[1] H. Stadler, F. Beggel, M. Habermehl, B. Persigehl, R. Kneer, M. Modigell, P. Jeschke, *Int. J. Greenhouse Gas Control* **2011**, *5*, 7.
[2] C. Zhang, J. Sunarso, S. Liu, *Chem. Soc. Rev.* **2017**, *46*, 2941.
[3] L. W. Tai, M. M. Nasrallah, H. U. Anderson, D. M. Sparlin, S. R. Sehlin, *Solid State Ionics* **1995**, *76*, 273.
[4] J. W. Stevenson, T. R. Armstrong, R. D. Carneim, L. R. Pederson, W. J. Weber, *J. Electrochem. Soc.* **1996**, *143*, 2722.
[5] S. P. Jiang, *Int. J. Hydrogen Energy* **2019**, *44*, 7448.
[6] X. Tan, N. Liu, B. Meng, J. Sunarso, K. Zhang, S. Liu, *J. Membr. Sci.* **2012**, *389*, 216.
[7] A. Berenov, A. Atkinson, J. Kilner, M. Ananyev, V. Eremin, N. Porotnikova, A. Farlenkov, E. Kurumchin, H. J. M. Bouwmeester, E. Bucher, W. Sitte, *Solid State Ionics* **2014**, *268*, 102.
[8] L. Wang, R. Merkle, J. Maier, T. Acartuerk, U. Starke, *Appl. Phys. Lett.* **2009**, *94*, 071908.
[9] D. Chen, Z. Shao, *Int. J. Hydrogen Energy* **2011**, *36*, 6948.
[10] Z. Shao, W. Yang, Y. Cong, H. Dong, J. Tong, G. Xiong, *J. Membr. Sci.* **2000**, *172*, 177.
[11] J. A. Kilner, R. J. Brook, *Solid State Ionics* **1982**, *6*, 237.
[12] R. D. Shannon, *J. Appl. Phys.* **1993**, *73*, 348.
[13] M. Arnold, H. Wang, A. Feldhoff, *J. Membr. Sci.* **2007**, *293*, 44.
[14] S. Engels, T. Markus, M. Modigell, L. Singheiser, *J. Membr. Sci.* **2011**, *370*, 58.
[15] D. S. Keeble, E. R. Barney, D. A. Keen, M. G. Tucker, J. Kreisel, P. A. Thomas, *Adv. Funct. Mater.* **2013**, *23*, 185.
[16] D. Schütz, M. Deluca, W. Krauss, A. Feteira, T. Jackson, K. Reichmann, *Adv. Funct. Mater.* **2012**, *22*, 2285.
[17] M. Li, M. J. Pietrowski, R. A. De Souza, H. Zhang, I. M. Reaney, S. N. Cook, J. A. Kilner, D. C. Sinclair, *Nat. Mater.* **2014**, *13*, 31.
[18] A. Wedig, R. Merkle, B. Stuhlhofer, H.-U. Habermeier, J. Maier, E. Heifets, *Phys. Chem. Chem. Phys.* **2011**, *13*, 16530.
[19] Y. Niu, J. Sunarso, F. Liang, W. Zhou, Z. Zhu, Z. Shao, *J. Electrochem. Soc.* **2011**, *158*, B132.
[20] K. Brinkman, T. Iijima, H. Takamura, *Solid State Ionics* **2010**, *181*, 53.
[21] D. Baek, A. Kamegawa, H. Takamura, *Solid State Ionics* **2014**, *262*, 691.
[22] V. Sadykov, N. Mezentseva, M. Arapova, T. Krieger, E. Gerasimov, G. Alikina, V. Pelipenko, A. Bobin, V. Muzykantov, Y. Fedorova, E. Sadovskaya, N. Eremeev, V. Belyaev, Y. Okhlupin, N. Uvarov, *Solid State Ionics* **2013**, *251*, 34.
[23] Q. Liao, Y. Wang, Y. Chen, Y. Wei, H. Wang, *J. Membr. Sci.* **2014**, *468*, 184.
[24] M. Colmont, M. Drache, P. Roussel, *J. Power Sources* **2010**, *195*, 7207.
[25] I. Arvanitidis, D. Siche, S. Seetharaman, *Metall. Mater. Trans. B* **1996**, *27*, 409.
[26] P. Taylor, S. Sunder, V. J. Lopata, *Can. J. Chem.* **1984**, *62*, 2863.
[27] N. Arora, G. Deo, I. E. Wachs, A. M. Hirt, *J. Catal.* **1996**, *159*, 1.
[28] S. Rothenberg, D. J. Payne, A. Bourlange, R. G. Egdell, *J. Appl. Phys.* **2007**, *102*, 113717.
[29] R. J. Walker, A. Pougin, F. E. Oropeza, I. J. Villar-Garcia, M. P. Ryan, J. Strunk, D. J. Payne, *Chem. Mater.* **2016**, *28*, 90.
[30] S. P. Tolochko, I. F. Kononyuk, L. S. Ivashkevich, A. S. Lyakhov, *Inorg. Mater.* **1993**, *29*, 1375.

[31] A. Wedig, R. Merkle, J. Maier, *J. Electrochem. Soc.* **2014**, *161*, F23.
[32] S. Huang, F. Gao, Z. Meng, S. Feng, X. Sun, Y. Li, C. Wang, *ChemElectroChem* **2014**, *1*, 554.
[33] D. S. Khaerudini, G. Q. Guan, P. Zhang, X. G. Hao, Z. D. Wang, Y. Kasai, K. Sasagawa, A. Abudula, *Int. J. Hydrogen Energy* **2015**, *40*, 11011.
[34] D. S. Khaerudini, G. Q. Guan, P. Zhang, X. G. Hao, Z. D. Wang, C. F. Xue, Y. Kasai, A. Abudula, *J. Power Sources* **2015**, *298*, 269.
[35] C. S. Knee, F. Lindberg, N. Khan, G. Svensson, P. Svedlindh, H. Rundlof, S. G. Eriksson, L. Borjesson, *Chem. Mater.* **2006**, *18*, 1354.
[36] A. K. Eriksson, F. Lindberg, G. Svensson, P. Svedlindh, P. F. Henry, S.-G. Eriksson, C. S. Knee, *J. Solid State Chem.* **2008**, *181*, 2031.
[37] D. A. Johnson, *Some Thermodynamic Aspects of Inorganic Chemistry*, 2nd ed., Cambridge University Press, Cambridge, UK **1982**, pp. 76–78.
[38] J.-I. Jung, S. T. Misture, D. D. Edwards, *Solid State Ionics* **2010**, *181*, 1287.
[39] A. A. Yaremchenko, D. D. Khalyavin, M. V. Patrakeev, *J. Mater. Chem. A* **2017**, *5*, 3456.
[40] S. J. Benson, R. J. Chater, J. A. Kilner, in *Proc. Third Int. Symp. Ionic and Mixed Conducting Ceramics*, Vol. *97-24* (Eds: T. A. Ramanarayanan, W. L. Worrell, H. L. Tuller, A. C. Khandkar, M. Mogensen, W. Gopel), Electrochemical Society, Pennington, NJ, USA **1998**, p. 596.
[41] T. Ishigaki, S. Yamauchi, K. Kishio, J. Mizusaki, K. Fueki, *J. Solid State Chem.* **1988**, *73*, 179.
[42] J. Druce, H. Tellez, M. Burriel, M. D. Sharp, L. J. Fawcett, S. N. Cook, D. S. McPhail, T. Ishihara, H. H. Brongersma, J. A. Kilner, *Energy Environ. Sci.* **2014**, *7*, 3593.
[43] C. V. Cushman, P. Brüner, J. Zakel, G. H. Major, B. M. Lunt, N. J. Smith, T. Grehl, M. R. Linford, *Anal. Methods* **2016**, *8*, 3419.
[44] H. H. Brongersma, M. Draxler, M. de Ridder, P. Bauer, *Surf. Sci. Rep.* **2007**, *62*, 63.
[45] J. Druce, T. Ishihara, J. Kilner, *Solid State Ionics* **2014**, *262*, 893.
[46] L. Wang, R. Merkle, Y. A. Mastrikov, E. A. Kotomin, J. Maier, *J. Mater. Res.* **2012**, *27*, 2000.
[47] Y. Hayamizu, M. Kato, H. Takamura, *J. Membr. Sci.* **2014**, *462*, 147.
[48] A. Vivet, P. M. Geffroy, E. Thune, C. Bonhomme, F. Rossignol, N. Richet, T. Chartier, *J. Membr. Sci.* **2014**, *454*, 97.
[49] Z. P. Shao, S. M. Haile, *Nature* **2004**, *431*, 170.
[50] M. Schulz, R. Kriegel, A. Kämpfer, *J. Membr. Sci.* **2011**, *378*, 10.
[51] E. P. Murray, M. J. Sever, S. A. Barnett, *Solid State Ionics* **2002**, *148*, 27.
[52] L. F. Nie, M. F. Liu, Y. J. Zhang, M. L. Liu, *J. Power Sources* **2010**, *195*, 4704.
[53] A. Esquirol, N. P. Brandon, J. A. Kilner, M. Mogensen, *J. Electrochem. Soc.* **2004**, *151*, A1847.